

Proceedings of the ASME 2019
**International Design Engineering Technical Conferences
 and Computers and Information in Engineering Conference
 IDETC/CIE2019**
August 18-21, 2019, Anaheim, CA, USA

DETC2019-97673

EXPERIMENTAL INVESTIGATIONS INTO BROADBAND VIBRATION ABSORPTION OF METASTRUCTURES WITH LATTICE DESIGNS

Joshua R. Tempelman*

Department of Mechanical Engineering
 Michigan State University
 East Lansing, MI 48824
 Email: tempelm2@egr.msu.edu

Melih C. Yesilli

Department of Mechanical Engineering
 Michigan State University
 East Lansing, MI 48824
 Email: yesillim@egr.msu.edu

Audun Myers

Department of Mechanical Engineering
 Michigan State University
 East Lansing, MI 48824
 Email: myersau3@egr.msu.edu

Firas A. Khasawneh

Department of Mechanical Engineering
 Michigan State University
 East Lansing, MI 48824
 Email: khasawn3@egr.msu.edu

ABSTRACT

Enhancements in manufacturing technologies, especially 3D-printing, have enabled the production of intricate micro-scale, elastic meta-structures. This study explores the broadband vibration absorption characteristics of these structures for three different geometries: simple-cubic periodic geometries as well as the more-involved diamond and octet-truss micro-lattice geometries. Broadband absorption is experimentally achieved for the basic cubic geometries with band gaps approximately 3000 Hz in width. A band gap of 3500 Hz is found in the octet-truss lattice with a 5% mass increase. The diamond lattice achieves a band gap width which doubles its cubic counterparts (6500 Hz), but only at a cost of a 4% mass increase. We compare the experimental findings to the theoretical results obtained by modeling the structure as a discrete, lumped mass system and employing modal analysis and transfer-function matrix methods. These comparisons show a mismatch between the theoretical and the experimental frequency responses. This mismatch is attributed to the inconsistencies inherent to 3D-printing processes, and to the need for more accurate modeling of the lattice structures.

INTRODUCTION

Micro-lattice geometries have been the topic of extensive research due to their exceptional strength-to-mass ratio [1–3]. This makes them an ideal candidate for applications with mass limitations such as vehicles and vessels as well as light-weight armor [4, 5]. Another advantage of lattice meta-structures is their ability to suppress vibration. Work on vibration suppression of these meta-structures has, until recently, focused on phononic crystals which are limited to high frequency and narrow band-gap applications such as acoustic cloaking [6] and sound absorption [7]. However, progress in materials and manufacturing have expanded the use of elastic meta-structures to more applications with wider frequency ranges.

Elastic meta-structures are characterized by a periodic geometry with an elastic media, and these structures typically include local resonators which suppress vibration. Since vibration caused by dynamic loading is undesirable in many engineering applications, metastructures' vibration absorption capabilities and light weight provide an alternative to traditional vibration absorbers [8].

High stiffness solid materials can also be used in vibration

*Address all correspondence to this author.

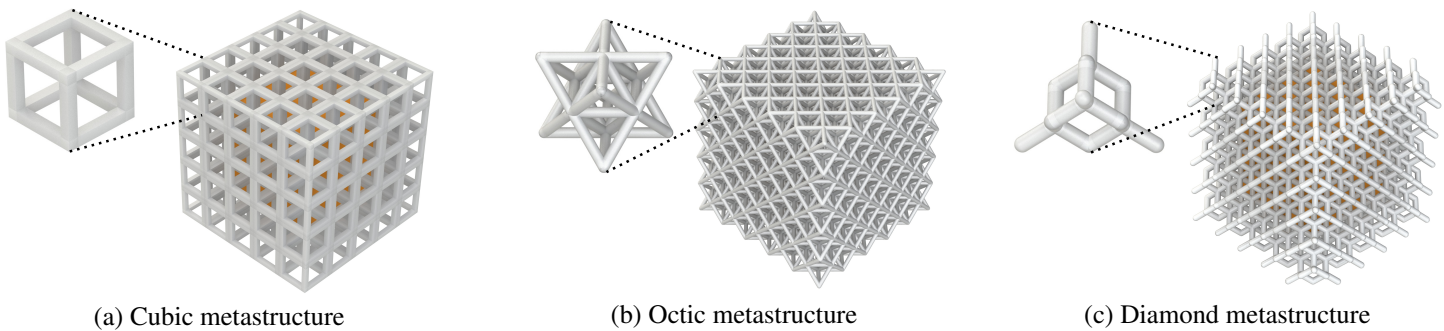


FIGURE 1: Some unit cells and example metastructures obtained by tessellating the unit cells.

isolation, however they lack the broad-band absorption capabilities of meta-structures and their modular design parameters [9]. Often times, engineered structures are excited over a wide range of frequencies, so it is best to design meta-materials that can attenuate vibration over a wide frequency range, or *band gap* [10]. Regions where these band gaps occur depend on the properties of the unit cell structure [11]. Therefore, the geometric design, material selection, and manufacturing method can all be used to tune the vibration absorption behavior of these structures [12].

Band gap formation for phononic crystals can be explained with Bragg scattering, and the locally resonant mechanism in metastructures produce the band gap formation in metamaterials [13]. Bragg scattering is based on Bragg condition and it can be explained with $f_{Bragg} = nv/2a$ given in [14] where f_{Bragg} , a , v and n represent, respectively, the center frequency of band gap, the lattice constant, the elastic velocity of the medium, and the cell number. Both Bragg scattering and the locally resonant mechanism can be observed in periodic structures , and the conditions for the transition between the two mechanisms were obtained by Liu and Hussein [15].

Matlack *et al.* [16] showed that the dynamic response of elastic meta-materials can be tuned to expand a structure's band gap based on the dimensions of simple-cube meta-material with embedded resonator masses. Their study also shows that increasing the lattice constant or decreasing the packing density of the resonator masses can lead to lower band gap frequencies. In this work, we reproduce the experimental methodology described in [16] and extend it to new lattice-based geometries.

Three geometric configurations of unit cells are used for the meta-structure prototypes. Namely, basic cubic, diamond, and octet-truss lattices are designed, manufactured, and tested. These unit cells are tessellated to obtain mesoscale unit cells with metallic resonators as in [16]. The unit cell configurations that we use and the corresponding mesoscale unit cells are provided in Fig. 1. We introduce equally-spaced cavities inside the mesoscale structure where we embed metallic resonators, see Fig. 3. Our metallic resonators are steel balls covered by 3D printed PLA structures to obtain cube dimensions. The purpose

of adding the metallic resonators is to produce the frequency band gaps for wave propagation of elastic waves inside the meta-structure [16]. The effect of cell geometry on abortion range is discussed in the section on broadband absorption behavior.

The simple-cubic meta-structure design shown in Fig. 1a was constructed for the low and high-stiffness configurations of the original study [16]. The high stiffness meta-structure is composed of the full tessellation of the unit cells. The low stiffness version is obtained by removing some of the links in the high stiffness meta-structure. Expanding beyond [16], this study also designs, manufactures, and tests intricate octet-truss and diamond micro-lattice meta-structures. In addition to the experimental work, we also derive an equation of motion for the structure by treating the embedded resonators as elastically connected lumped masses. The frequency response of the resulting structures is obtained by performing frequency sweeps on a piezoelectric shaker, and is compared to the results of modal analysis and the transfer matrix method.

MANUFACTURING PROCEDURE

This section outlines how we manufactured the piezoelectric shaker fixture, and the metastructures. To begin the manufacturing process, the piezoelectric shaker fixture, base plate, and twelve cubic casing halves (Fig. 3) were 3D printed using a QIDI Tech printer (Tab. 2-line 1) with PLA plastic, a 0.4 mm nozzle, 20% infill, and 0.2 mm layer height. Next, six steel spheres with 7/16" diameter between two cubic casing halves are placed and adhered together using Loctite 454 adhesive gel to create a total of six cubic resonators as shown in Fig. 3. The metastructures are then 3D-printed using PLA plastic with 100% infill and 0.15 mm layer height to the point shown in Fig. 3. The print is paused at this point and the resonators are placed in the cubic cavities with Loctite 454 adhesive gel on three sides of the resonator to increase bonding to the metastructure. When all resonators are placed, the print is resumed. For assembling the manufactured components please see Section .

The lattice dimensions were determined by the printing lim-

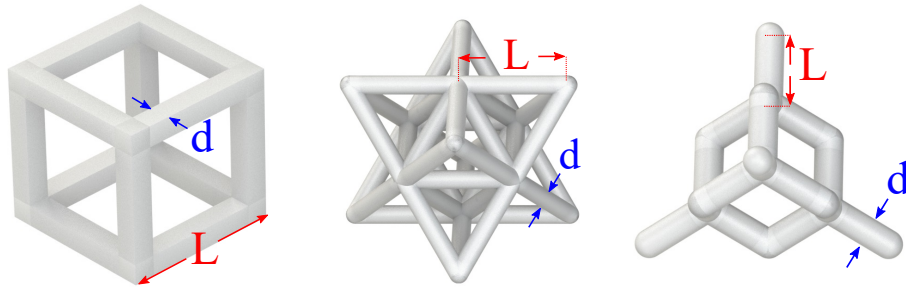


FIGURE 2: Dimensions reference for single cell lattice structure: (left) Cubic, (middle) Diamond, and (right) Octic.

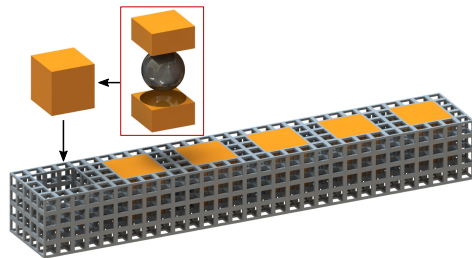


FIGURE 3: Assembly process for embedding resonators during 3D printing of meta-structure: Cubic casings glued together with embedded steel sphere and cubic resonators inserted into meta-structure during 3D printing.

iterations of an introductory 3D printer (Tab. 2-line 1) with a 0.4 mm nozzle and 0.15 mm layer height. The listed dimensions and masses (including the embedded resonators) for each unit cell are provided in Tab. 1, see Fig. 2 for the corresponding schematic.

TABLE 1: Single cell dimensions for lattice structures.

| Lattice | L (mm) | d (mm) | m (gram) including resonator mass |
|---------|--------|--------|---|
| Cubic | 0.5500 | 4.0333 | Low stiffness: 47.0 High stiffness: 47.3 |
| Diamond | 0.8500 | 1.8000 | 49.2 |
| Octic | 0.6500 | 2.8992 | 49.5 |

EXPERIMENTAL PROCEDURE

This section describes how we set up the experiment and how we collected the acceleration data both at the base and top of the metastructures over a frequency sweep.

We first secured the piezoelectric shaker (Tab. 2-line 2) between the two 3D printed fixture clamps by tightening the clamp bolts (1/4" × 20) to approximately 5 Nm (Fig. 4). Next, the four base bolts (Fig. 4) are tightened to approximately 20 Nm to securely attach the fixture to an optical table.

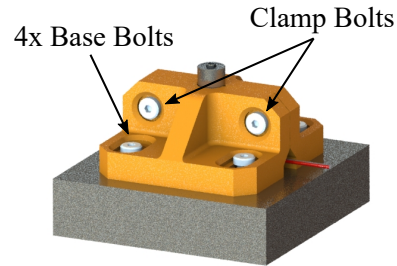


FIGURE 4: Mount assembly for the piezo shaker.

To attach the metastructure to the shaker, the base plate (Fig. 7-2) is fastened to the shaker using an M3 bolt (M3 × 0.5mm × 10mm) tightened to approximately 5 Nm. The bottom of the metastructure is then attached to the base plate using adhesive wax (Tab. 2 - line) as shown in Fig. 7-3. Finally, with the meta-structure in place, two uni-axial accelerometers (Tab. 2-line 5) are attached to the top of the metastructure and underneath the base plate (Fig. 7-4). The resulting experimental apparatus is shown in Fig. 5.

To begin the data collection, the Data Acquisition device (DAQ), (Tab. 2-line 8), signal generator (Tab. 2-line 4), signal conditioner (Tab. 2-line 6), amplifier (Tab. 2-line 3), and Shaker (Tab. 2-line 2) are connected according to Fig. 6.

Data is then collected using the MATLAB® data acquisition toolbox on a personal PC (Tab. 2-line 9) with a sampling rate of 500 kHz over 35 seconds. Before starting the recording, we set the signal generator for a sine wave linear frequency sweep ranging from 1 Hz to 10 kHz with a 3.5 V offset and 1 V

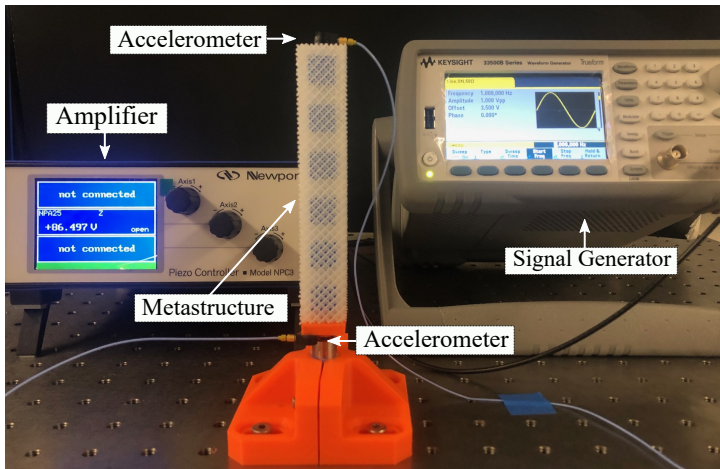


FIGURE 5: Physical experimental setup for performing a frequency sweep using the diamond lattice structure.

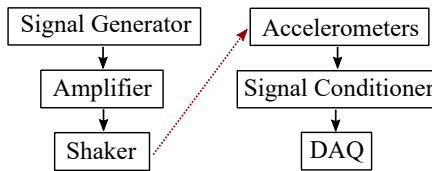


FIGURE 6: Connectivity diagram for collecting acceleration data from metastructures.

amplitude (peak to peak) over 30 seconds.

Equipment

Table 2 lists all of the equipment that we used in this study. The QIDI Tech X-one 3D printer is used for manufacturing the metastructures. The selected material for our prints is a PLA filament with a diameter of 1.75 mm and a printer nozzle diameter of 0.4 mm. The bed temperature was set to 50°C and the nozzle temperature was set to 200°C. The infill percent for each 3D printed component is listed in Section .

The Newport NPA25 Nano-positioning piezoelectric actuator is used to excite the metastructure. This actuator has 25 μm travel range, 1000 N axial load capacity, and its resonant frequency is 12 kHz. This actuator is used with Newport NPC3 Nano-positioning amplifier. A Keysight 33511B signal generator is used to provide the input signals to the amplifier for the piezoelectric actuator.

Vibration measurement on the meta-structures are taken using two uni-axial accelerometers. More specifically, PCB Model 352A24 accelerometers were attached to the metastructure as shown in Fig. 7-4. Model 080A109 Petro wax was used to attach the accelerometers to the metastructures which have a resonant frequency of 65 kHz. The National Instruments NI USB-6356

DAQ is used to take data from experimental setup, and the DAQ was directly connected to a Dell OptiPlex 7050 computer to collect the data using the MATLAB® data acquisition toolbox.

TABLE 2: Equipment used in this project

| |
|-------------------------------------|
| QIDI Tech X-one 3D printer |
| NPA25 Piezoelectric Actuator |
| NPC3 Open-loop Amplifier |
| Keysight 33511B Signal Generator |
| PCB Model 352A24 Accelerometer |
| PCB Model 482C15 Signal Conditioner |
| Model 080A109 Petro Wax |
| NI USB-6356 DAQ |
| Dell OptiPlex 7050 Computer |

PARAMETER ESTIMATION

To approximate the spring stiffness for the resonators \hat{k} and the metastructure k from Fig. 9, a finite element model is employed. Specifically, we used SolidWorks' built in finite element module for static applications on a single cubic metastructure (Fig. 8) with an embedded steel cube. The metastructure material properties are defined to be the built-in PLA material but with a change of the modulus of elasticity to 3.33 GPa as suggested by Letcher and Waytashek [17] for 3D printed PLA. The properties of the embedded masses were set to those of plain carbon steel. To determine the resonator stiffness \hat{k} , the spring constants from compression (Fig. 8-A and B) and the flexural stiffness (Fig. 8-C) resisting the resonator from translation are superimposed. Furthermore, the bottom surface of the metastructure is fixed from translation in the vertical direction and a force of 1 N is applied to the top of the cube. This results in a stiffness of $\hat{k} = 5.19 \text{ MN/m}$ and 92.3 MN/m for the low and high stiffness metastructures, respectively. To determine the structure stiffness k , we applied a compression test on the outside shell of the metastructure (Fig. 8-D) resulting in the stiffness $k = 1.11 \text{ MN/m}$.

DISCRETE ANALYSIS METHODS

There are several models for analyzing elastic meta structures. One must choose whether to treat the system as a continuum or as a discrete set of harmonic oscillators. Here we chose to discretize the structure into a lumped parameter system with a series of tuned-mass-dampers (TMDs) as shown in Fig. 9. The resulting equations of motion should be a set of $2n + 1$ differential equations where n is the number of local resonators. This simplification enables obtaining a closed-form solution. We use the

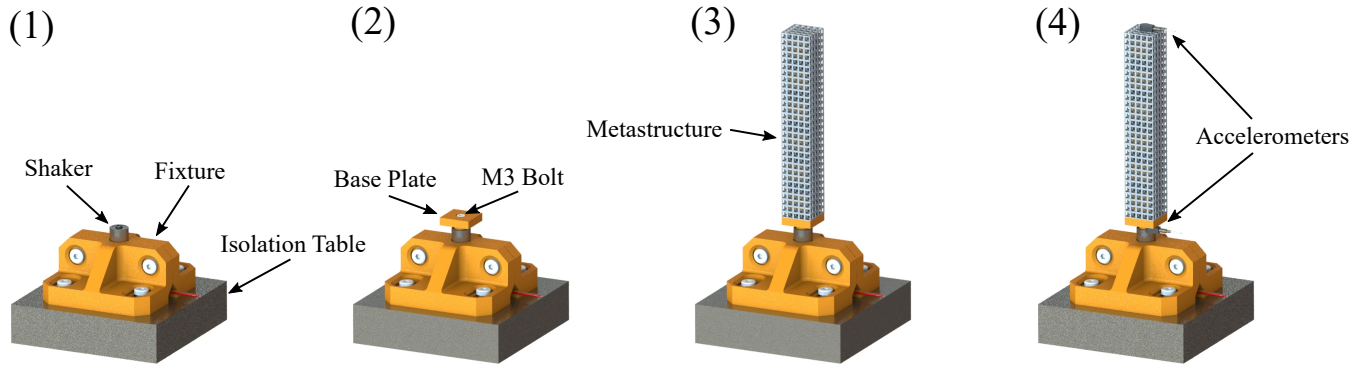


FIGURE 7: Assembly process for attaching meta-structure to shaker. (A) attaching fixture to table, (B) attaching base plate to shaker (C) adhering meta-structure to base plate using wax (D) adhering accelerometers to meta-structure using wax.

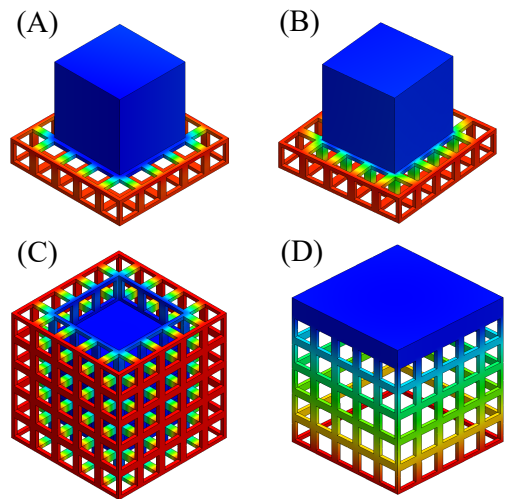


FIGURE 8: FE displacement models for approximations of the stiffness of cubic lattice metastructure with 1 N load: (a) low stiffness compression (b) high stiffness compression, (c) flexural deflection, and (d) external shell compression. The resulting stiffness: $k_A = 0.87 \text{ MN/m}$, $k_B = 9.23 \text{ MN/m}$, $k_C = 4.32 \text{ MN/m}$, and $k_D = 1.11 \text{ MN/m}$.

traditional modal analysis method as well as the transfer-matrix method described in [18] to solve the simplified system.

EQUATIONS OF MOTION

For repeating structures like ours, patterns in the equations of motion may be easily obtained through Newton's second law [19]. Free-body diagrams can be constructed for each element to account for the forces acting on the mass element as a function of the element's position, velocity, and acceleration. Constructing a free-body diagram for some interior mass element m_i with position x_i and attached local resonator \hat{m}_i , \hat{x}_i , a

pair of general equations of motion are constructed. With damping temporarily ignored, the resulting equations of motion for this arbitrary mass element and attached local resonator are

$$m_i \ddot{x}_i = k(x_{i-1} - x_i) + k(x_{i+1} - x_i) + \hat{k}(\hat{x}_i - x_i), \quad (1a)$$

$$\hat{m}_i \ddot{\hat{x}}_i = \hat{k}(x_i - \hat{x}_i), \quad (1b)$$

where (\cdot) and $(\ddot{\cdot})$ denote the first and second time derivatives, respectively. All the other Mass-TMD pairs in the structure are governed by the same equation with the exception of the first and last masses which are in contact with one main spring. Hence, it is a straight-forward process to construct the general stiffness matrix for a metastructure modeled in this manner. Defining $\tilde{k} = 2k + \hat{k}$, the general form of the stiffness matrix for n resonators is given by

$$\mathbf{K} = \begin{bmatrix} \tilde{k} & -k & 0 & \dots & 0 & 0 & 0 & -\hat{k} & 0 & 0 & \dots & 0 & 0 & 0 \\ -k & \tilde{k} & -k & \dots & 0 & 0 & 0 & 0 & -\hat{k} & 0 & \dots & 0 & 0 & 0 \\ 0 & -k & \tilde{k} & \dots & 0 & 0 & 0 & 0 & 0 & -\hat{k} & \dots & 0 & 0 & 0 \\ \vdots & \vdots & \vdots & \ddots & \vdots & \vdots & \vdots & \vdots & \vdots & \vdots & \ddots & \vdots & \vdots & \vdots \\ 0 & 0 & 0 & \dots & \tilde{k} & -k & 0 & 0 & 0 & 0 & \dots & -\hat{k} & 0 & 0 \\ 0 & 0 & 0 & \dots & -k & \tilde{k} & -k & 0 & 0 & 0 & \dots & 0 & -\hat{k} & 0 \\ 0 & 0 & 0 & \dots & 0 & -k & \tilde{k} & 0 & 0 & 0 & \dots & 0 & 0 & 0 \\ -\hat{k} & 0 & 0 & \dots & 0 & 0 & 0 & \hat{k} & 0 & 0 & \dots & 0 & 0 & 0 \\ 0 & -\hat{k} & 0 & \dots & 0 & 0 & 0 & 0 & \hat{k} & 0 & \dots & 0 & 0 & 0 \\ 0 & 0 & -\hat{k} & \dots & 0 & 0 & 0 & 0 & 0 & \hat{k} & \dots & 0 & 0 & 0 \\ \vdots & \vdots & \vdots & \ddots & \vdots & \vdots & \vdots & \vdots & \vdots & \vdots & \ddots & \vdots & \vdots & \vdots \\ 0 & 0 & 0 & \dots & -\hat{k} & 0 & 0 & 0 & 0 & 0 & \dots & \hat{k} & 0 & 0 \\ 0 & 0 & 0 & \dots & 0 & -\hat{k} & 0 & 0 & 0 & 0 & \dots & 0 & \hat{k} & 0 \\ 0 & 0 & 0 & \dots & 0 & 0 & -\hat{k} & 0 & 0 & 0 & \dots & -0 & 0 & \hat{k} \end{bmatrix}, \quad (2)$$

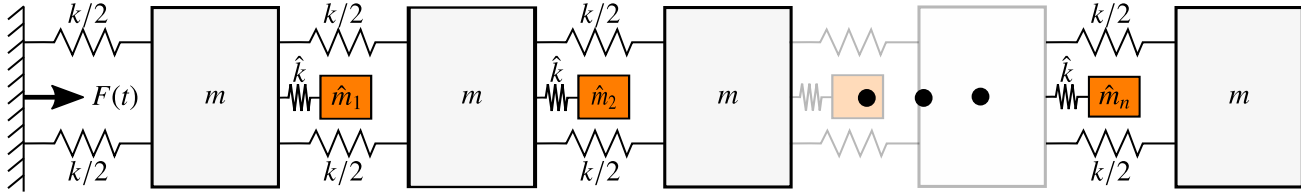


FIGURE 9: Discrete model of a metastructure.

which corresponds to the position vector \mathbf{X} and mass matrix \mathbf{M} according to

$$\mathbf{x} = [x_1, x_2, \dots, x_{n+1}, \dot{x}_1, \dot{x}_2, \dots, \dot{x}_n]^T, \quad (3)$$

$$\mathbf{M} = \text{diag}([m_1, m_2, \dots, m_{n+1}, \hat{m}_1, \hat{m}_2, \dots, \hat{m}_n]). \quad (4)$$

The structural damping is not easily resolved, and it is common practice in structural dynamics to define the damping matrix \mathbf{D} to be arbitrarily proportional to the stiffness matrix [20] according to $\mathbf{D} = \alpha \mathbf{K}$. With the inclusion of the damping matrix, the homogeneous equations of motion for the unforced system read

$$\mathbf{M}\ddot{\mathbf{x}} + \mathbf{D}\dot{\mathbf{x}} + \mathbf{K}\mathbf{x} = \mathbf{0}. \quad (5)$$

MODAL ANALYSIS

Modal analysis is a widely used method in vibration analysis for discretized models [21]. For the undamped case, the solution takes the form $\mathbf{x} = \mathbf{u}e^{i\omega t}$. Nontrivial solutions for \mathbf{u} give the squared natural frequencies and mode shapes of the structure. These are obtained by solving the Eigenvalue problem $|\mathbf{K} - \omega^2 \mathbf{M}| = 0$.

The eigenvectors are stored in a modal matrix, \mathbf{X} . The mode shapes are then anthropologized with respect to the mass mode shape i.e. $\mathbf{X}^T \mathbf{M} \mathbf{X} = \mathbf{I}$. Using the expansion theorem the response may be written as a combination of the normal modes

$$\mathbf{x}(t) = \mathbf{X}\mathbf{q}(t) \quad (6)$$

where \mathbf{q} is a column matrix of generalized coordinates. Now the equations of motion become

$$\mathbf{X}^T \mathbf{M} \mathbf{X} \ddot{\mathbf{q}} + \mathbf{X}^T \mathbf{K} \mathbf{X} \mathbf{q} = \mathbf{X}^T \mathbf{F} = \mathbf{Q}, \quad (7)$$

where \mathbf{Q} is the generalized force vector corresponding to the generalized coordinates \mathbf{q} . It follows that the equations of motion can be written in terms of their generalized coordinates as

$$\ddot{\mathbf{q}}(t) + 2\zeta \omega_n \dot{\mathbf{q}}(t) + \omega_n^2 \mathbf{q}(t) = \mathbf{Q}(t). \quad (8)$$

The resulting set of equations are $2n + 1$ uncoupled differential equations of the second order. These uncoupled equations may be treated a set of single degree of freedom systems with a known solution form

$$q_i(t) = e^{-\zeta \omega_{nt} t} q_i(0) \cos \omega_i t + \left(e^{-\zeta \omega_{nt} t} \frac{\dot{q}_i(0)}{\omega_i} \right) \sin \omega_i t + \frac{1}{\omega_i} \int_0^T Q_i(\tau) \sin \omega_i(t - \tau) d\tau. \quad (9)$$

TRANSFER MATRIX METHOD

It has been shown in prior metastructure research [18] that a transfer matrix may be constructed for discrete models. This transfer matrix can be used to analytically compute the H_2 and H_∞ performance measures which are related to the total and the maximum energies of the system, respectively. Though these norms originated in control theory, it has been shown these can be used as a performance measure when designing TMDs for multi degree of freedom systems [22]. To set up the transfer matrix, use the definitions of Eqs. (4) and (10) to define new matrix functions which convert the equations into the state-space form

$$\mathbf{A} = \begin{bmatrix} \mathbf{0} & \mathbf{I} \\ -\mathbf{M}^{-1} \mathbf{K} & -\mathbf{M}^{-1} \mathbf{D} \end{bmatrix}, \quad \mathbf{B} = \begin{bmatrix} \mathbf{0} \\ -\mathbf{M}^{-1} \end{bmatrix}, \quad \mathbf{C} = [\mathbf{I} \ \mathbf{0}]. \quad (10)$$

The transfer matrix for the system is then given as

$$\mathbf{H}(s) = \mathbf{C} (s\mathbf{I} - \mathbf{A})^{-1} \mathbf{B} = \begin{bmatrix} H_{11}(s) & \dots & H_{1n}(s) \\ \vdots & \ddots & \vdots \\ H_{n1}(s) & \dots & H_{nn}(s) \end{bmatrix}. \quad (11)$$

The transfer matrix $\mathbf{H}(s)$ gives $G(s) = H_{nn}(s)$. This is the response of the last term in the transfer function matrix that reveals the relationship between the input and the response at the tip of the structure. The $G(s)$ term provides the force transmissibility which can be thought of as the gain of a control loop. The modal analysis method is compared to the transfer matrix method in Fig. 10 where it is shown that the frequency response of the two

methods are in agreement. It should be noted that the authors found the two methods to be less compatible as damping estimates grew excessively high.

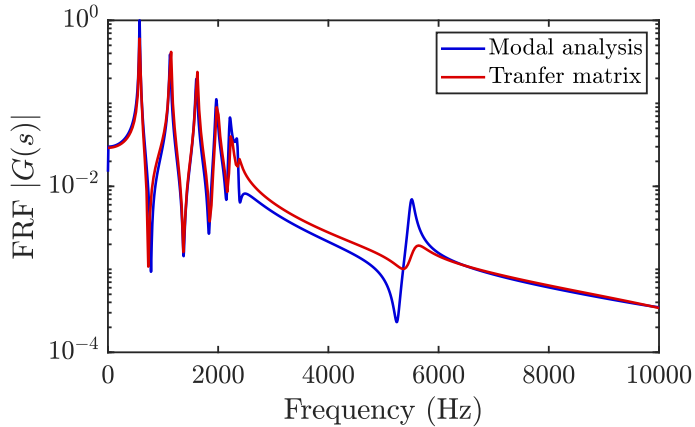


FIGURE 10: The comparison of the frequency responses for both the modal analysis and transfer matrix methods.

RESULTS

Acceleration data was collected at both the base and the tip of the metastructures during frequency sweeps between 1 Hz and 10 kHz. For the analysis in this study, only the dynamic response at the tip of the structure is considered. The raw time-series recorded from the frequency sweeps are given in Fig. 11 for our four structures. The data was collected over a span of 35 seconds for a 30 second frequency sweep, so these series were truncated to exclude data prior to and following the sweep. A visual inspection of the time-series leads to the conclusion that the peak response for the structures occurs during the first few seconds of the sweep during low-frequency excitation. The elevations in amplitude for the time response of the structures corresponds to elevations in the power level in frequency domain. The last noticeable elevation in amplitude of the diamond structure occurs later than what is shown for the competing configurations indicating that it is the stiffest structure (higher-frequency resonance), which is confirmed by Fourier analysis. Note that six separate frequency sweeps were conducted for each structure, and the average power level across these six data sets is reported. This is done to ensure the reported findings are consistent and repeatable.

We used the modal analysis method to generate analytic models for the response of the low-stiffness and high-stiffness structures. The analytic models of the cubic structures seem to be in general agreement with experimental data. Fig. 12 shows

the peak responses of the analytic models do not land on the same frequencies as the experimental data, but the broad-band absorption behavior of experimental data seems to follow, to some degree, the analytic model. The transfer-function matrix approach was also used to compare theoretical to experimental results. The peak frequencies of the transfer matrix approach align with peak frequencies of the modal analysis approach and the absorption range fits well with experimental data. The transfer function evaluation shows more realistic absorption behavior as it does not make excessive drops in the power levels.

Comparing the analytic model to the experimental data, it is clear that the stiffness values used for the model are too high. The peak frequencies for the analytic results occur at slightly higher frequencies than the experimental data, and the broadband absorption gaps seem to be slightly shifted to high-frequency regions for the analytic model. We also note that the analytic model predicts far greater vibration suppression in the broad-band gap than what is experimentally achievable. This discrepancy was also seen for the low-stiffness models in [16], and it may be explained by an assortment of uncertainties which present themselves in an experimental environment. For instance, the 3D de-

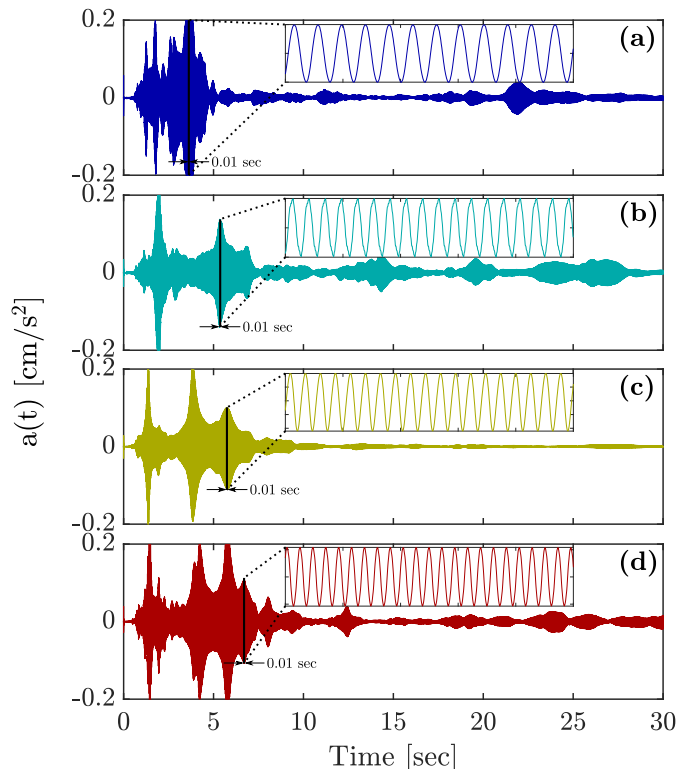


FIGURE 11: The time-series of the dynamic response to frequency sweep excitation from a 1 Hz to 10 kHz for the (a) low-stiffness and (b) high-stiffness basic cubic structures, (c) octet-truss lattice structure, and (d) diamond lattice structure.

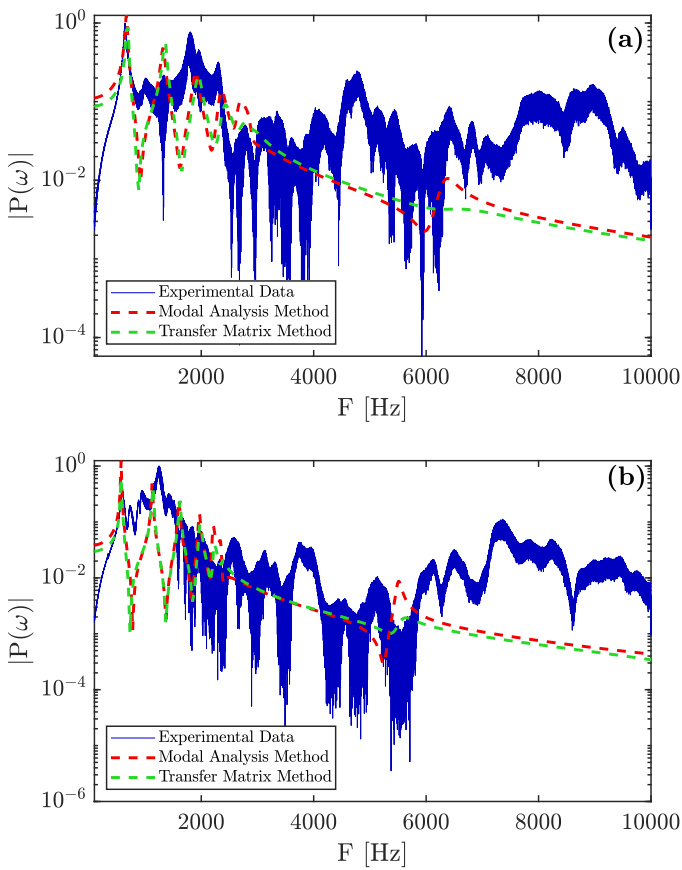


FIGURE 12: A comparison of the modal analysis technique (dashed red) and transfer matrix method (dashed green) to experimental data for (a) the high-stiffness structure and (b) low-stiffness structure.

position printing method used in this experiment may lead to a structure which is not isotropic and homogeneous, seriously altering its physical properties. Additionally, the analytic study does not consider the added masses of the accelerometers. To complicate experimental results further, it is impossible to conclude that the transmission of the force between the piezo-shaker and the base of the structure is not distorted by the attachment mechanism used to secure the structure on the testing rig. Further, the effect of noise must be considered as well.

BROADBAND ABSORPTION BEHAVIOR

The broad-band absorption behavior varies considerably between different structures. For this experiment, the absorption behavior is categorized by a gap in the frequency response of the data for which it is apparent that modal responses are being suppressed and the power level is sufficiently lower than what is seen for its neighboring frequencies. The visible interpretations

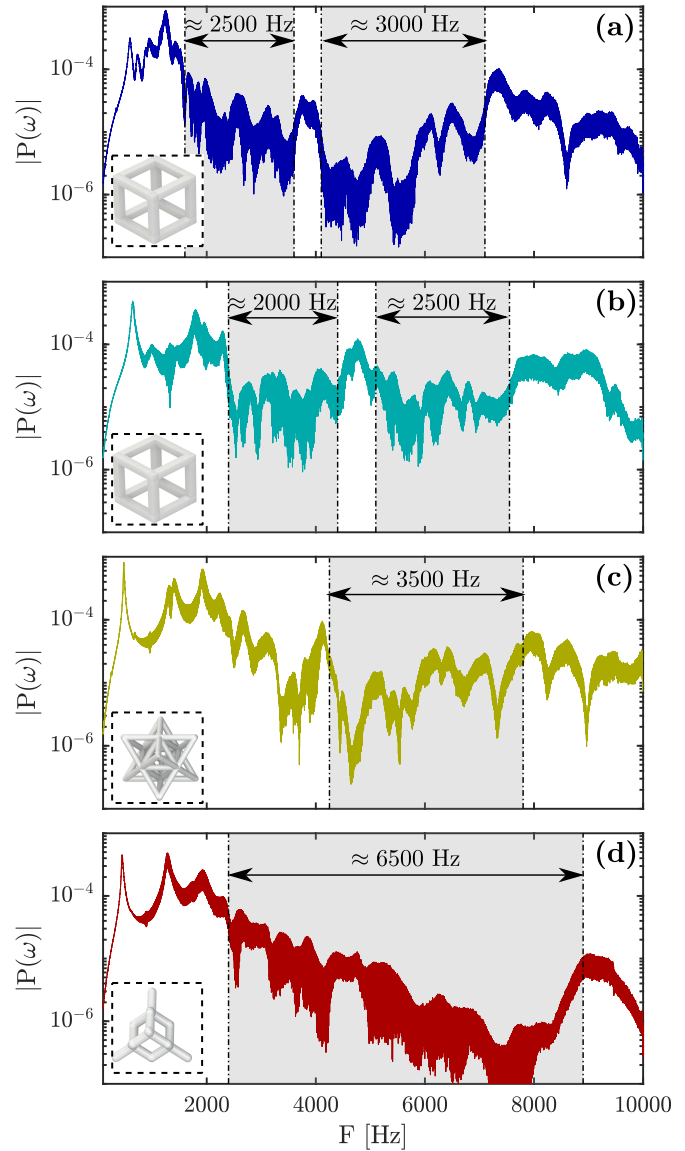


FIGURE 13: The broad-band absorption behavior shown in gray for (a) the low-stiffness simple-cubic structure, (b) high-stiffness simple-cubic structure, (c) octet-truss lattice structure and (d) diamond lattice structure.

of this phenomenon are seen in the frequency responses shown in Fig. 13 with overlaid gray-scaled regions to indicate an absorption range. Here, the frequency responses are normalized, and we focus on the relative power levels.

The low-stiffness cubic structure has its band gaps at the lowest frequencies of the four structures. The power levels of this structure are suppressed between 1600 to 3600 Hz as well

as between 4100 to 7100 Hz. These band gaps are large enough to claim that the structure has achieved broadband absorption. The high-stiffness cubic structure performs very similarly to its low-stiffness counterpart, but with band gaps at higher frequencies. The two distinct absorption ranges for this structure occur between 2400 to 4400 Hz and 5100 to 7550 Hz. The size of these ranges is very close to the low stiffness model. The absorption ranges of the high-stiffness structures in this study mirror the results of low-stiffness structures in [16], which is not surprising since this study used a lower-stiffness material for the manufacturing of the metastructures.

Looking at the lattice-based geometries, the performance deviates from the cubic counterparts. A noticeable band gap emerges for the octet-truss structure between 4250 to 7800 Hz. There is a narrow frequency band where the power level is suppressed for this structure in the low frequency range (3500 to 3700 Hz), but this band is not wide enough to be considered broadband. Thus, the uninterrupted bandwidth of the octet-truss exceeds that of both the low-stiffness and high-stiffness cubic structures whose longest uninterrupted absorption range is 3000 Hz. This is done at a cost of a 5% increase in mass.

On the other hand, the diamond lattice performs exceptionally well. A clear suppression of the power level is shown in Fig. 13 over the range of 2400 to 89000 Hz. This structure behaves like a higher-stiffness rendition of the cubic based structures, but with little cost in added mass. The uninterrupted band-gap is essentially doubled in this structure compared to its cubic counterparts, but only at a cost of a 4% increase in mass. Thus, it is shown that a modification to the print geometry can be used to tune the performance of these structures without making serious compromises to the total structure mass.

CONCLUSIONS

In this work, we have shown the manufacturing methodology, testing procedure, and basic modeling tools for investigating both simple and sophisticated metastructure designs. The findings of show resemblance to the results found in [16] in the sense that broadband vibration suppression was realized with metastructures. The PLA material used in this study resulted in absorption behavior more indicative of low-stiffness structures used in [16] which is to be expected considering the discrepancy in stiffness compared to previous work using poly-carbonate.

The transfer-function matrix analysis method and modal analysis methods are applied to generate comparative theoretical results, and it is shown that theoretical performance deviates from experimental data as peak frequencies are misaligned from analytic to experimental frequency response. However, the models do predict absorption behavior for the same general frequency ranges found in the experimental data, although the agreement is in the broad qualitative sense (Fig. 12). This indicates that the dynamic response of the resonators is roughly captured by the

lumped-mass modeling technique.

Additionally, new lattice-based designs are introduced as possible high-performance metastructures which tune absorption behavior through their geometry rather than by simply adding mass to alter stiffness. The octet-truss and diamond lattice structures are printed and embedded with resonators, and their absorption behavior was revealed through frequency-sweep testing, the results of which are shown in Fig. 13. A noticeable 3500 Hz band gap emerges in the octet-truss structure which is larger than the uninterrupted band gaps seen for cubic geometries, and this comes at the cost of a 5% mass increase (47.3 versus 49.5 grams). The diamond lattice design has a band gap of 6500 Hz which is approximately double that of the 3000 Hz band gap shown for its cubic counterpart (Fig.13). Furthermore, this is achieved with only a 4% mass increase (47.3 versus 49.2 grams).

The findings of this study could be bolstered if a printer with higher resolution is used. The geometry of the diamond lattice was constrained by the printers resolution, thus limiting the ability to explore lighter options with similar absorption behavior. Furthermore, the entry level printer used in this study had difficulty producing clean links in the octet-truss structure, and manufacturing with a more advanced printer would likely augment the dynamic response. We also echo the conclusion in [18] for the need of more accurate models for meatstructures than the lumped mass technique.

REFERENCES

- [1] Yan, C., Hao, L., Hussein, A., Bubb, S. L., Young, P., and Raymont, D., 2014. “Evaluation of light-weight AlSi10mg periodic cellular lattice structures fabricated via direct metal laser sintering”. *Journal of Materials Processing Technology*, **214**(4), apr, pp. 856–864.
- [2] Hou, A., and Gramoll, K., 1998. “Compressive strength of composite lattice structures”. *Journal of Reinforced Plastics and Composites*, **17**(5), mar, pp. 462–483.
- [3] Yan, C., Hao, L., Hussein, A., and Raymont, D., 2012. “Evaluations of cellular lattice structures manufactured using selective laser melting”. *International Journal of Machine Tools and Manufacture*, **62**, nov, pp. 32–38.
- [4] Moon, S. K., Tan, Y. E., Hwang, J., and Yoon, Y.-J., 2014. “Application of 3d printing technology for designing light-weight unmanned aerial vehicle wing structures”. *International Journal of Precision Engineering and Manufacturing-Green Technology*, **1**(3), jul, pp. 223–228.
- [5] Ma, Z.-D., 2009. Lightweight composite armor, Feb. 17. US Patent 7,490,539.
- [6] Liang, Y.-J., Chen, L.-W., Wang, C.-C., and Chang, I.-L., 2014. “An acoustic absorber implemented by graded index phononic crystals”. *Journal of Applied Physics*, **115**(24), p. 244513.
- [7] Zhang, X., Qu, Z., He, X., and Lu, D., 2016. “Experi-

- tal study on the sound absorption characteristics of continuously graded phononic crystals". *AIP Advances*, **6**(10), p. 105205.
- [8] Syam, W. P., Jianwei, W., Zhao, B., Maskery, I., Elmadih, W., and Leach, R., 2018. "Design and analysis of strut-based lattice structures for vibration isolation". *Precision Engineering*, **52**, apr, pp. 494–506.
- [9] Elmadih, W. A., Syam, W. P., Maskery, I., and Leach, R., 2017. "Additively manufactured lattice structures for precision engineering applications". In 32nd Annual Meeting of the American Society for Precision Engineering.
- [10] Zouari, S., Brocail, J., and Génevaux, J.-M., 2018. "Flexural wave band gaps in metamaterial plates: A numerical and experimental study from infinite to finite models". *Journal of Sound and Vibration*, **435**, nov, pp. 246–263.
- [11] Ampatzidis, T., Leach, R., Tuck, C., and Chronopoulos, D., 2018. "Band gap behaviour of optimal one-dimensional composite structures with an additive manufactured stiffener". *Composites Part B: Engineering*, **153**, nov, pp. 26–35.
- [12] Ozdemir, Z., Hernandez-Nava, E., Tyas, A., Warren, J. A., Fay, S. D., Goodall, R., Todd, I., and Askes, H., 2016. "Energy absorption in lattice structures in dynamics: Experiments". *International Journal of Impact Engineering*, **89**, mar, pp. 49–61.
- [13] Hussein, M. I., Leamy, M. J., and Ruzzene, M., 2014. "Dynamics of phononic materials and structures: Historical origins, recent progress, and future outlook". *Applied Mechanics Reviews*, **66**(4), may, p. 040802.
- [14] Yu, D., Wen, J., Zhao, H., Liu, Y., and Wen, X., 2008. "Vibration reduction by using the idea of phononic crystals in a pipe-conveying fluid". *Journal of Sound and Vibration*, **318**(1-2), nov, pp. 193–205.
- [15] Liu, L., and Hussein, M. I., 2012. "Wave motion in periodic flexural beams and characterization of the transition between bragg scattering and local resonance". *Journal of Applied Mechanics*, **79**(1), p. 011003.
- [16] Matlack, K. H., Bauhofer, A., Krödel, S., Palermo, A., and Daraio, C., 2016. "Composite 3d-printed metastructures for low-frequency and broadband vibration absorption". *Proceedings of the National Academy of Sciences*, **113**(30), pp. 8386–8390.
- [17] Letcher, T., and Waytashek, M., 2014. "Material property testing of 3d-printed specimen in PLA on an entry-level 3d printer". In Volume 2A: Advanced Manufacturing, ASME.
- [18] Reichl, K. K., and Inman, D. J., 2017. "Lumped mass model of a 1d metastructure for vibration suppression with no additional mass". *Journal of Sound and Vibration*, **403**, sep, pp. 75–89.
- [19] Rao, S., 1986. *Mechanical Vibrations*. Addison Wesley Longman Publishing Co.
- [20] Gawronski, W. K., 2004. *Advanced Structural Dynamics and Active Control of Structures*. Springer-Verlag GmbH.
- [21] Meirovitch, L., 1967. *Analytical Methods in Vibrations*. Pearson.
- [22] Hadi, M. N. S., and Arfiadi, Y., 1998. "Optimum design of absorber for MDOF structures". *Journal of Structural Engineering*, **124**(11), nov, pp. 1272–1280.